Avalanches triggered by Kelvin-Helmholtz instability in a cylindrical plasma device

Y. Lang,[1,*] Z. B. Guo,[1] X. G. Wang,[1] and B. Li[2,†]
[1]*Fusion Simulation Center, School of Physics, Peking University, Beijing 100871, China*
[2]*School of Physics, Beihang University, Beijing 100191, China*

(Received 13 June 2019; published 26 September 2019)

A profile-evolving simulation of the Controlled Shear Decorrelation Experiment (CSDX) linear device is performed with our newly developed code. The simulation result shows an excellent agreement with the experimental observations of profiles and fluctuations of plasma density and electric potential in the $B = 1000$ G standard discharges, suggesting the mechanism of their evolutions. According to our simulation, an avalanche of plasma density, featuring a rapid destruction of particle profile, is triggered every time the dominant instability transits from near adiabatic collisional drift wave to non-adiabatic Kelvin-Helmholtz instability. The avalanches always start at the point where the local vorticity is the maximum among the whole device. A critical vorticity is found for any avalanche to happen. The avalanches always lead to intermittent particle and heat convective structures outside the main plasma column, and these structures are ejected out as avaloids when zonal flow intensity at birth time is weak.

DOI: 10.1103/PhysRevE.100.033212

I. INTRODUCTION

From low temperature cylindrical laboratory plasma devices to toroidal fusion devices, boundary intermittent convective structures, known as blobs [1], filaments [2] and avaloids [3], are observed to dominate particle and heat transport outside the bulk plasma. In tokamaks, the smaller ones, called blobs, are believed to be beneficial because they enlarge the plasma wetted area of the limiter/divertor targets, and thus alleviate local target heat load. However, the bigger ones, called edge localized mode (ELM) filaments, are believed to be harmful since they can damage the first wall severely. Consequently, the birth of these structures at the edge of main plasma is of wide interest.

For the birth of blobs and ELM filaments in tokamaks, quantitatively comparing simulations with experiments can be really hard, in that a simulation model to cover the complex physics across a tokamak separatrix is still not good enough, and that a sufficient global high-resolution diagnostics of the tokamak edge is currently unavailable. These difficulties are rather easy to overcome in linear devices like the Controlled Shear Decorrelation Experiment (CSDX), which share similar scaling properties [4] with tokamak boundaries but do not have magnetic curvature, magnetic shear, magnetic separatrix, equilibrium current, neoclassical effects, hot ions, and various impurities, and thus the mechanisms should be simpler. In tokamaks and linear devices, avaloids are intermittent convective structures outside the main plasma, moving radially outward but remaining connected to the main plasma, with large spacial scale (turbulence macroscale) and large radial velocity (the order of 1/10th of sound speed) [3]. Although avaloids in CSDX share similarities with ELM filaments in tokamaks [3,5], how much its mechanism can be adapted to tokamak boundary convective events still requires further investigation. What draws our special interest is that CSDX is equipped with insulating endplates, thus eliminating radial current conduction by walls, and is in this sense a better test bed to study tokamak edge physics.

In CSDX, experiments show that the fluctuations inside and outside the main plasma column have a distinct relation [3]. That is, a necessary condition for an avaloid to eject is that the main plasma transits from a poloidal mode number $m \geqslant 3$ dominated phase to an $m = 1$ dominated phase, and the $m = 1$ mode amplitude exceeds some threshold. Later more explanations are given about these two phases, naming the $m \geqslant 3$ dominated phase shear flow growth phase and the other collapse phase [6], which is the way we refer to them in this paper. These observations suggest that the transition between modes is key to understand the birth of the transport events we are interested in.

Experiments suggest that the transition phenomenon is the result of the turbulence modulated by bursting azimuthal flow, and the flow modifies the density gradient significantly [7]. Previously two 2D (two-dimensional) codes [8,9] and one 3D code [10] were used to simulate plasma behavior in CSDX. All of them fix density profiles as the particle source and sink, forbidding $m = 0$ evolutions. However, these simulations suffer from equilibrium density gradient uncertainties, because equilibrium density steepening stiffly affects the turbulence saturation level [11]. These motivated us to build a source-driven code that evolves full parameters. The code leads to the conclusion that the $m = 1$ mode is a Kelvin-Helmholtz (K-H) instability, which results in the avalanche of plasma density, that is, a fast-growing destruction of density profile.

Previous simulations suggest that high enough zonal flow shear intensity [12] or preexisting perturbation amplitude [13] can result in the onset of an ELM. Our code shows that, in CSDX, Kelvin-Helmholtz (K-H) instability triggered

*ylang@pku.edu.cn
†plasma@buaa.edu.cn

avalanches always result in violent loss of confinement, and the lost plasma can be radially transported in the form of avaloids outside the main plasma region. An avalanche always happens when and where the local vorticity w exceeds a critical value, which contains the contrition of both zonal flow shear and preexisting perturbation. In this paper we study the birth of avaloids, and the result may provide insights into the birth criterion of intermittent convective structures like blobs and ELM filaments in tokamaks.

II. SIMULATION MODEL

Our simulation model is based on the drift-reduced Braginskii equations for magnetized plasma [14] with cold ions. Quasineutrality and electrostatic conditions are used. We choose the electrostatic simulation model because CSDX is a low-β device and the drift turbulence is shown to be electrostatic [15]. A detailed derivation of our model equations is given in Appendix A, and the proof of the corresponding energy conservation is given in Appendix B.

To obtain the dimensionless equations, the density n is normalized to n_0; electron temperature T_e to T_0; electric potential ϕ to T_0/e; velocities, including the $\boldsymbol{E}\times\boldsymbol{B}$ velocity $\boldsymbol{v}_E$, ion parallel velocity $v_{\parallel i}$, and electron parallel velocity $v_{\parallel e}$, are normalized to $c_{s0}=\sqrt{T_0/m_i}$; time to $t_0=a/c_{s0}$; parallel length to $L_\parallel$ and perpendicular length to $\rho_{s0}=c_{s0}/\Omega_i$, where a and $L_\parallel$ are the radius and height of the cylindrical vacuum. The background magnetic field in CSDX is approximated to be constant, $\boldsymbol{B}=B\hat{\boldsymbol{z}}$, so that the ion gyrofrequency $\Omega_i=eB/(m_ic)$ is also constant. We have shown (see Appendix C) that magnetic perturbations perpendicular to the dominant magnetic field direction are negligible by solving $\nabla\times\boldsymbol{B}_\perp=j_\parallel\hat{\boldsymbol{z}}$ in the code. Expressed in normalized symbols, the model equations are

$$d_tT_e=-\frac{2}{3}T_e\nabla_\parallel v_{\parallel e}+\chi_\perp\nabla_\perp^2T_e+\chi_\parallel\nabla_\parallel^2T_e-\gamma T_e+S_{T_e}, \quad (1)$$

$$d_tn=-\nabla_\parallel(nv_{\parallel e})+D_\perp\nabla_\perp^2n+D_\parallel\nabla_\parallel^2n-\gamma n+S_n, \quad (2)$$

$$d_tv_{\parallel i}=-\frac{T_e}{n}\nabla_\parallel n+\mu_\perp\nabla_\perp^2v_{\parallel i}+\mu_\parallel\nabla_\parallel^2v_{\parallel i}-\nu_{i,n}v_{\parallel i}, \quad (3)$$

$$d_tw=\frac{1}{n}\nabla_\parallel j_\parallel+\mu_\perp\nabla_\perp^2w+\mu_\parallel\nabla_\parallel^2w-\nu_{i,n}w, \quad (4)$$

where $d_t=\partial_t+(a/\rho_{s0})\boldsymbol{v}_E\cdot\nabla$, $\boldsymbol{v}_E=\boldsymbol{b}\times\nabla\phi$, $\nabla_\parallel=(a/L_\parallel)\partial_z$. The vorticity of $\boldsymbol{E}\times\boldsymbol{B}$ velocity, i.e., $w\hat{\boldsymbol{z}}\equiv\nabla\times\boldsymbol{v}_E$, is written in the normalized form as

$$w\equiv\nabla_\perp^2\phi. \quad (5)$$

S_{Te} and S_n are explicit temperature and ion sources, assumed to have the form

$$S_n(r)=0.5S_{n0}\left[1-\tanh\left(\frac{r-r_0}{d}\right)\right], \quad (6)$$

$$S_{T_e}(r)=0.5S_{T_e0}\left[1-\tanh\left(\frac{r-r_0}{d}\right)\right]. \quad (7)$$

In experiments the sources of density and temperature provided by helical antenna increase along the $\hat{\boldsymbol{z}}$ direction, but their radial and axial distributions are unknown [16]. In the form of sources we guess above, we intentionally set the sources axially uniform to eliminate axial monotonic variation of electron pressure, which can be a drive of self-amplifying axial flow [17,18] and the underlying physics is beyond the interest of this paper. The sink of the density and temperature of the plasma in the system is determined by the balance between ionization and recombination processes, which is roughly estimated by the γ terms. The collisional coupling between ions and neutrals provides a momentum sink, and this effect is estimated by the $\nu_{i,n}$ terms, where $\nu_{i,n}$ is the ion-neutral collision frequency. A better understanding of the damping effect by neutrals can be found elsewhere [18]. $\chi_\parallel$ is estimated according to the classical (Spitzer) parallel heat conduction density [19],

$$\chi_\parallel n_0\frac{dT_e}{dz}\Big/\frac{\mathrm{eV}}{\mathrm{cm^2s}}\approx-q_{\parallel\mathrm{cond}}\Big/\frac{\mathrm{eV}}{\mathrm{cm^2s}}$$
$$=1.25\times10^{20}\left(\frac{T_e}{\mathrm{eV}}\right)^{5/2}\frac{dT_e}{dz}\Big/\frac{\mathrm{eV}}{\mathrm{cm}}. \quad (8)$$

$D_\parallel$ and $\mu_\parallel$ terms are used to damp high $k_\parallel$ modes that we cannot resolve in our code. $D_\perp$ and $\chi_\perp$ are updated locally by classical diffusion

$$D_\perp=\chi_\perp$$
$$=1.625\times10^{-5}\frac{n}{\mathrm{cm^{-3}}}\left(\frac{T_e}{\mathrm{eV}}\right)^{-\frac{3}{2}}\left(\frac{B}{\mathrm{G}}\right)^{-2}\ln\Lambda_0\ \mathrm{cm^2/s}, \quad (9)$$

where $\ln\Lambda_0$ is the Coulomb logarithm calculated using n_0 and T_0 instead of the local density and temperature, for numerical simplicity. We use the estimation of mean ion-ion viscosity $\mu_\perp$ by the generalized Braginskii formula [10]. Parallel current is normalized to en_0c_{s0} and is given by the parallel Ohm's law

$$j_\parallel=\frac{1}{\nu_*}(\nabla_\parallel p_e-n\nabla_\parallel\phi), \quad (10)$$

where $\nu_*=t_0\nu_{e,i}m_e/m_i$. $\nu_{e,i}$ is the electron-ion collision frequency updated locally by

$$\nu_{e,i}=2.906\times10^{-6}\ln\Lambda_0\frac{n}{\mathrm{cm^{-3}}}\left(\frac{T_e}{\mathrm{eV}}\right)^{-3/2}\mathrm{Hz}. \quad (11)$$

The normalized electron parallel velocity is thus given by

$$v_{\parallel e}=v_{\parallel i}-j_\parallel/n. \quad (12)$$

Similar model equations have been used for the study of turbulence and transport in the Large Plasma Device (LAPD) [20,21].

Our simulation domain is the whole CSDX device. We use a Cartesian (x,y,z) coordinate, whose z increases along the magnetic field line. We choose $x=0$, $y=0$ to be at the center of the cylindrical vacuum vessel, and $z=0$ at the end plate with a glass window [16]. This allows us to express the perpendicular convection terms in Poisson brackets:

$$\boldsymbol{v}_E\cdot\nabla f=\frac{\partial\phi}{\partial x}\frac{\partial f}{\partial y}-\frac{\partial\phi}{\partial y}\frac{\partial f}{\partial x}\equiv[\phi,f]. \quad (13)$$

A diagram of the simulation grid is shown in Fig. 1. We use a cylindrical zero perpendicular boundary condition. That is, all

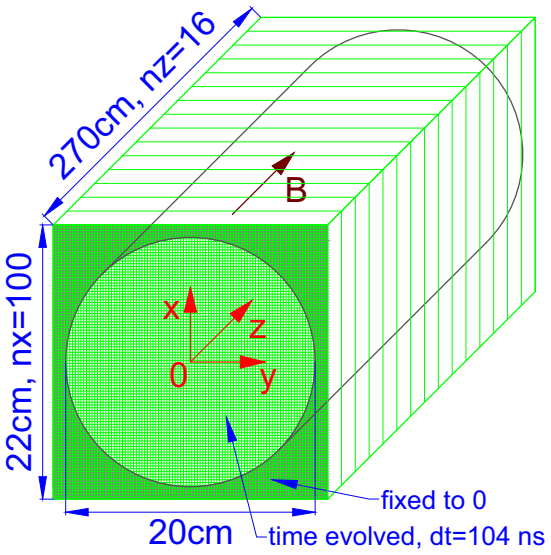

FIG. 1. Diagram of the simulation domain. Equations (1) to (4) are advanced in the $r = 10$ cm cylinder. The view angle of an operational fast camera is used [16].

fields at the grid points outside the vessel ($r = \sqrt{x^2 + y^2} > a$) are fixed to be zero, so that the variables are evolved only inside the vacuum vessel. In this paper we focus on experiments with insulating end plates, so we use periodic boundary conditions at z boundaries to eliminate differences between different x-y planes. Experiments have shown that the parallel wavelength of the turbulence is comparable to the length of the device [10,22], and this is also the case in our simulation results. The model equations are solved by a finite-difference turbulence code with centered difference in space and a predictor-corrector scheme for time stepping [23]. The Poisson equation (5) is solved by a parallel 2D finite difference solver, with cylindrical zero boundary condition. We always start the simulations with no plasma and very small initial random noise. We force $T_e \geqslant 0.004T_0$ and $n \geqslant 0.004n_0$ for numerical feasibility. The time step is chosen to be $dt = 1.04 \times 10^{-4}$ ms. We have run separate cases with orders of magnitude greater initial perturbations, double time-step width, and half perpendicular grid size to ensure convergence.

In this paper, we use $T_0 = 3$ eV, $n_0 = 1 \times 10^{13}$ cm^{-3}, $a = 10$ cm, $L_\parallel = 270$ cm, $\mu_\perp = 5.36 \times 10^3$ cm^2/s, $D_\parallel = \mu_\parallel = 7 \times 10^6$ cm^2/s, $\chi_\parallel = 1.9 \times 10^8$ cm^2/s, $\gamma = 5 \times 10^3$ Hz, $\nu_{i,n} = 3.4 \times 10^3$ Hz, $r_0 = 3$ cm, $d = 0.55$ cm, $B = 1000$ G.

III. TURBULENCE PERIOD

For the convenience of analysis, we convert the output data from Cartesian grid to cylindrical grid. Scalars are interpolated to cylindrical grid points, and vectors are decomposed to $\boldsymbol{v} = v_r\hat{\boldsymbol{r}} + v_\theta\hat{\boldsymbol{\theta}}$. This allows us to define and calculate zonal average and perturbation by

$$\langle f \rangle = \int_0^{L_\parallel}\int_0^{2\pi} f(r,\theta,z)d\theta\, dz,$$
$$\tilde{f}(r,\theta,z) = f - \langle f \rangle. \tag{14}$$

To avoid confusion, it is helpful to mention here that, in most of the CSDX experimental papers, $\tilde{f}$ refers to the fluctuations of f, which is the deviation from the equilibrium f_0, and f_0 is time independent [11], allowing the zonal average of fluctuations to be nonzero, which is different from what we define as perturbations. For the decomposition of different azimuthal mode numbers, we use the notation

$$\Phi_m(r,z) \equiv \frac{1}{2\pi}\int_0^{2\pi} \phi(r,\theta,z)e^{-im\theta}d\theta \equiv |\Phi_m|e^{iS_{\phi,m}}. \tag{15}$$

In this way,

$$\phi(r,\theta,z) = \sum_{m=-\infty}^{\infty} \Phi_m e^{im\theta}$$
$$= 2\sum_{m=1}^{\infty} |\Phi_m|\cos(m\theta + S_{\phi,m}) + \Phi_0, \tag{16}$$

so any scalar field can be expressed by the summation of different modes given by

$$\phi_m(r,\theta,z) \equiv 2|\Phi_m|\cos(m\theta + S_{\phi,m}), \quad m = 1, 2, \ldots, \infty. \tag{17}$$

In order to understand the onset of avalanches, we need to introduce the whole picture of a standard discharge. The evolution of plasma behavior is observed in some aspects, but most of the experimental reports only show time-averaged or frequency-filtered results. We describe our simulation of the whole periodic evolution and compare with experiments.

As mentioned in Sec. I, each period is separated into two phases. Fig. 2 shows how the intensity of $m = 3$ and $m = 1$ perturbations evolves with respect to zonal flow. It is clear that basically $m = 3$ dominates over $m = 1$ when shear flow grows, and $m = 1$ dominates over $m = 3$ when shear flow collapses. This phenomenon has been confirmed by experiments [6] and is used to distinguish the two phases. We have to say that although the driving of $m = 1$ perturbation is relatively clear (as will be explained later), the damping of it is determined by recombination, which is considered rather roughly in our code. This can result in some error of the simulated $m = 1$ mode lifetime.

IV. SHEAR FLOW GROWTH PHASE

We choose the beginning of a period to be the shear flow growth phase. This phase is vital to this paper because it determines the onset of K-H instability. A typical one is chosen here for detailed analysis. Other shear flow growth phases are basically the same because they share the same density and temperature sources, but may vary a little since each one of them is influenced by the collapse phase just before it.

A. Early shear flow growth phase

A shear flow growth phase starts by a linear growth of a collisional drift wave (CDW) [24], which we refer to as the early shear flow growth phase. Density and temperature sources produce gradients, driving the CDW to grow. We judge this instability to be a CDW by testing the conditions of a CDW in a linear device given in [16,25]. Figure 3(a)

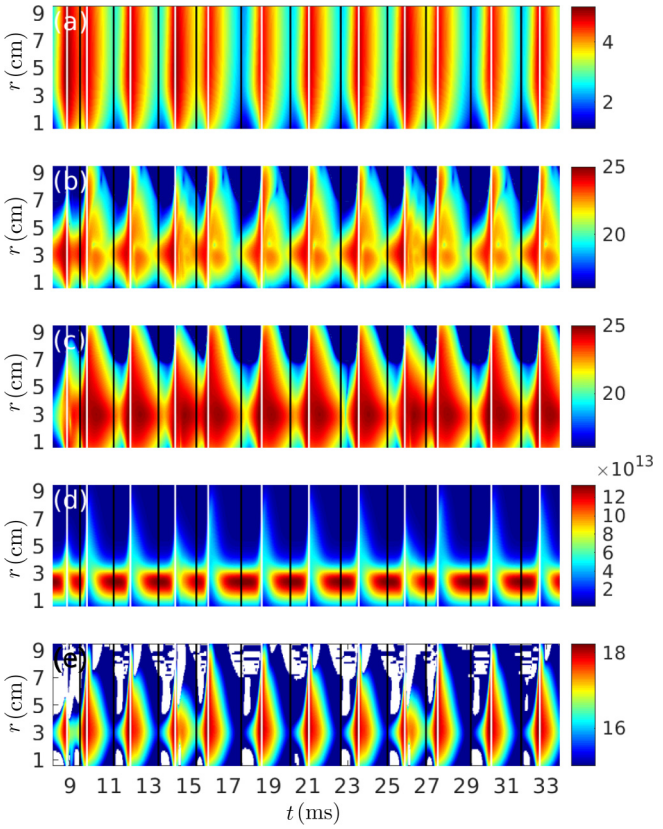

FIG. 2. Simulation result of the evolution of (a) zonal flow $\lg\langle v_{E,\theta}/(\mathrm{cm/s})\rangle$, (b) $m = 3$ perturbation autopower $\lg\langle(\tilde{n}_3/\mathrm{cm}^{-3})^2\rangle$, (c) $m = 1$ perturbation autopower $\lg\langle(\tilde{n}_1/\mathrm{cm}^{-3})^2\rangle$, (d) particle count radial distribution $\langle 2\pi r\, n/\mathrm{cm}^{-2}\rangle$, (e) outward radial particle convection $\lg\langle 2\pi r\, n v_{E,r}/(\mathrm{cm}^{-2}\mathrm{cm/s})\rangle$ (left white for inward particle flux regions). We use same color bar for different azimuthal mode numbers of perturbations for comparison. We use the same dark blue color for regions where $\langle\tilde{n}_m^2\rangle \leqslant 10^{16}$ cm^{-6} and $0 < 2\pi r\langle n v_{E,r}\rangle \leqslant 10^{15}$ cm^{-2}cm/s, in case of miscalibration of the color bars due to some trivial low values. Vertical white and black lines show the times when zonal flow at $r = 3$ cm starts to decrease and increase respectively, labeling phase transition times.

shows that its dominant azimuthal mode number m is 3, independently of radial location. This $m = 3$ perturbation has a typical CDW helical structure, rotating in electron diamagnetic drift direction. The phase velocity at $r = 3.6$ cm can thus be estimated using Fig. 3 by

$$v_{\mathrm{ph}} = \frac{\omega_r}{k_\theta} = \frac{\omega_r r}{m} \approx 4.42 \times 10^4 \ \mathrm{cm/s}. \tag{18}$$

Referring to Fig. 2(a), one can figure out that in early shear flow growth phase, the flow velocity is negligible compared to CDW phase velocity, which means CDW phase velocity is the same in the laboratory frame as in the plasma frame at the time. Hereafter v_{ph} is used to denote the phase velocity of CDW in the plasma frame. This velocity determines the lowest azimuthal velocity of $m = 3$ fluctuations at $r = 3.6$ cm, since the plasma $\boldsymbol{E} \times \boldsymbol{B}$ flow velocity is always in the electron diamagnetic drift direction, as shown in Fig. 2(a). The exact definition of a camera-seen azimuthal velocity, noted by v_θ, and its evolution at $r = 3.6$ cm can be found in [7], mentioned

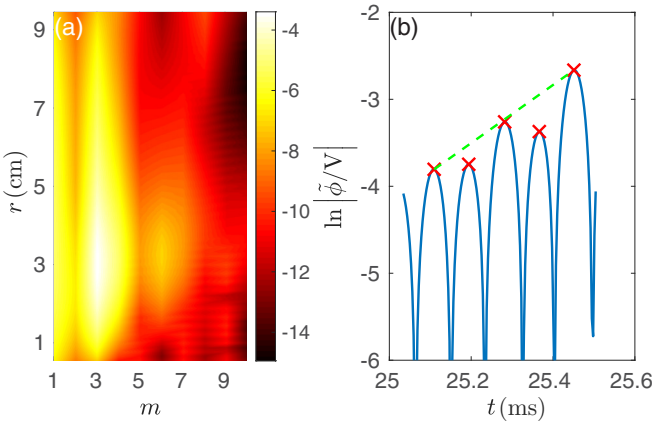

FIG. 3. Simulation result of early shear flow growth phase features a linear growth of a CDW. (a) Zonal-averaged auto-spectrum of electric potential perturbation $\lg\langle\tilde{\phi}_m^2/\mathrm{V}^2\rangle$ at $t = 25.19$ ms. (b) Evolution of perturbed electric potential at a certain position at $r = 3.6$ cm. The green line connects the beginning and ending of two adjacent CDW periods, whose incline is used to estimate linear growth rate $\gamma = 3.34$ ms^{-1} and interval is used to estimate real frequency $f = \omega_r/2\pi \approx 5.86$ kHz.

above. Our simulations show that the phase velocity of a linear CDW (electron diamagnetic velocity shifted by some additional effects included in our equations) can successfully explain the minimum azimuthal velocity observed by a fast camera, in spite of several negative spikes. These spikes always appear at late collapse phases, when the dominant perturbation may be either $m \geqslant 3$ or $m = 1$. Of course $m = 1$ perturbations are not part of a linear CDW, but can influence 2D time-delay estimation (TDE) analysis on camera data in [7].

B. Late shear flow growth phase

As the nonlinear terms grow to be comparable to linear terms, the system enters the late shear flow growth phase. This is directly reflected by the shift of the CDW phase velocity from the plasma frame to the laboratory frame, which means that the azimuthal convection of the CDW by zonal flow is no longer negligible. The azimuthal motion of the $m = 3$ fluctuation is accelerated to $v_\theta \approx \langle v_{E,\theta}\rangle + v_{\mathrm{ph}}$. The growth of zonal and parallel flows is shown in Fig. 4. The generation mechanisms of these flows have been studied intensively both experimentally and theoretically, but our simulation analyses on these topics are not ready to be published yet.

For direct comparison with experiments and a clear illustration of phase transition times, the blue curve in Fig. 5(a) shows the evolution of zonal flow at $r = 3.6$ cm. One finds that the heights of the peaks and the intervals between peaks in our simulation result are very close to those observed in experiments [7]. The simulation of the total shear flow growth phase provides a reasonable explanation of fast-camera observations of zonal-averaged increases in azimuthal velocity. To our knowledge, the most recently published observation of a $\langle v_{E,\theta}\rangle$ profile [26], which is a time-averaged result, agrees with our simulation result well. Experimental observations of high frequency fluctuations ($f \geqslant 6$ kHz)

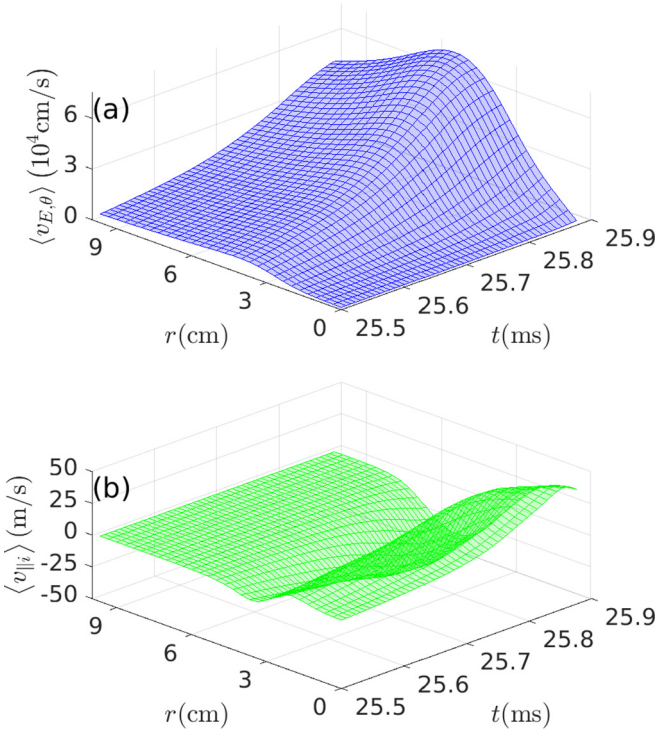

FIG. 4. Late shear flow growth phase features a significant growth of both (a) zonal flow $\langle v_{E,\theta}\rangle$ and (b) radially sheared parallel flow $\langle v_{\|i}\rangle$.

in $B = 1000$ G discharges exhibit broadband autospectra [27,28]. According to our simulation, we infer that this feature is a result of the acceleration of an $m = 3$ dominated mode by growing $\boldsymbol{E} \times \boldsymbol{B}$ flow. To experimentally verify our inference, a wavelet analysis for a shear flow growth phase is required.

After the validation study above, here we introduce some of the features in shear flow growth phases observed in our simulation. Although $m = 3$ perturbations dominate this phase, other mode number components, especially $m = 2$ and $m = 4$ components, are not negligible, and can affect the transition from shear flow growth phase to collapse phase. Other features are shown in Fig. 2. Until the end of a whole shear flow growth phase, the density profile remains stable, providing a necessary condition for the CDW to grow roughly linearly in the plasma frame. In this phase, the growth of the CDW is accompanied by the growth of radial particle flux, at $r \approx 3$ cm. This magnetic flux surface has the maximum density gradient, consistent with experiments. Previously we divided the late shear flow growth phase from the early phase by the condition of $\langle v_{E,\theta}\rangle \lesssim v_{\rm ph}$. This is almost the same time when $\langle \tilde{n}_1^2\rangle$ starts growing. The total flow intensity grows accordingly, accumulating free energy for the onset of K-H instability.

V. COLLAPSE PHASE

In this section we focus on the collapse phase, i.e., the $m = 1$ dominated phase. Because the source driving the whole system is zonal, $m = 1$ perturbations will finally get dissipated. The system then returns to the shear flow growth phase.

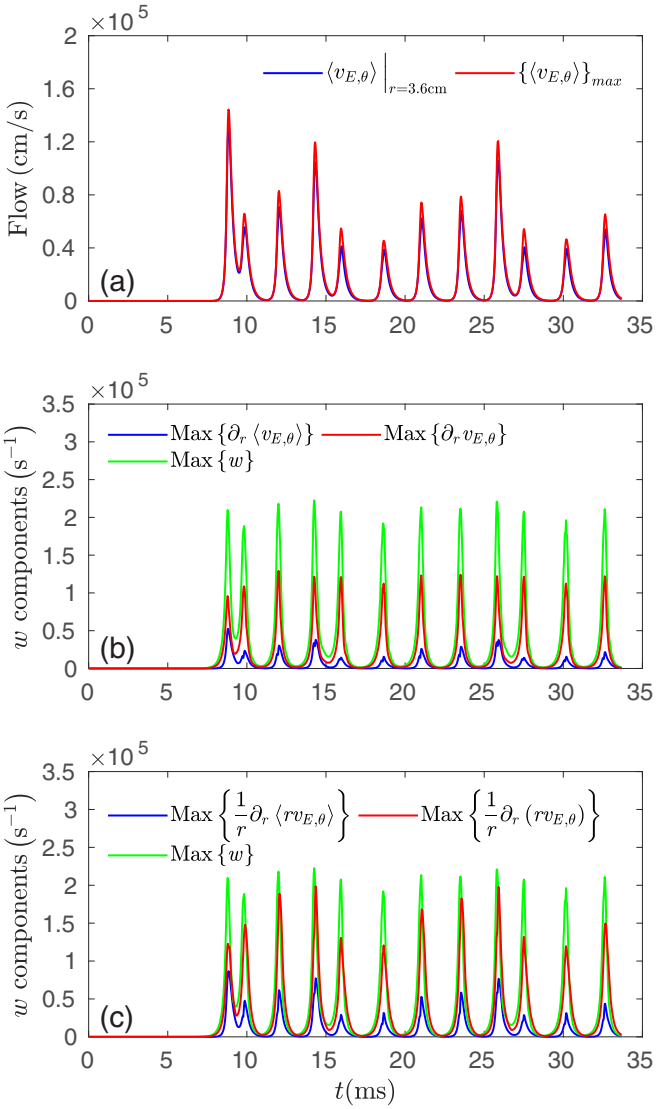

FIG. 5. Evolution of key scalars in the whole case. (a) is the zonal-averaged azimuthal $\boldsymbol{E} \times \boldsymbol{B}$ velocity at $r = 3.6$ cm and the global maximum, indicating the time of transitions between two phases. (b) is the global maximum vorticity contribution by the radial shear of $\boldsymbol{E} \times \boldsymbol{B}$ velocity $\hat{\boldsymbol{r}} \times \partial_r \boldsymbol{v}_E$, compared to maximum total vorticity. (c) is the maximum vorticity contribution by the curl of azimuthal $\boldsymbol{E} \times \boldsymbol{B}$ velocity $\nabla \times (v_{E,\theta}\hat{\boldsymbol{\theta}})$, compared to maximum total vorticity. The global maximum of a scalar f, Max$\{f\}$, is the maximum f evaluated in the region 0.5 cm $\leqslant r \leqslant$ 9.5 cm.

A. Basic phenomenon

Zonal flow can be nonlinearly damped through K-H instability [29]. Experiments suggest that the dominant instability outside the main plasma column is K-H instability [16]. It is natural to infer that in our case K-H instability is responsible for the collapse of shear flow.

The cross-phase of two scalar fields is defined by

$$\xi_m\langle n, \phi\rangle(r, z) \equiv S_{n,m}(r, z) - S_{\phi,m}(r, z). \tag{19}$$

Two typical transitions from shear flow growth phase to collapse phase are shown in Figs. 6 and 7, where one can clearly see the dominant azimuthal mode number of both density and

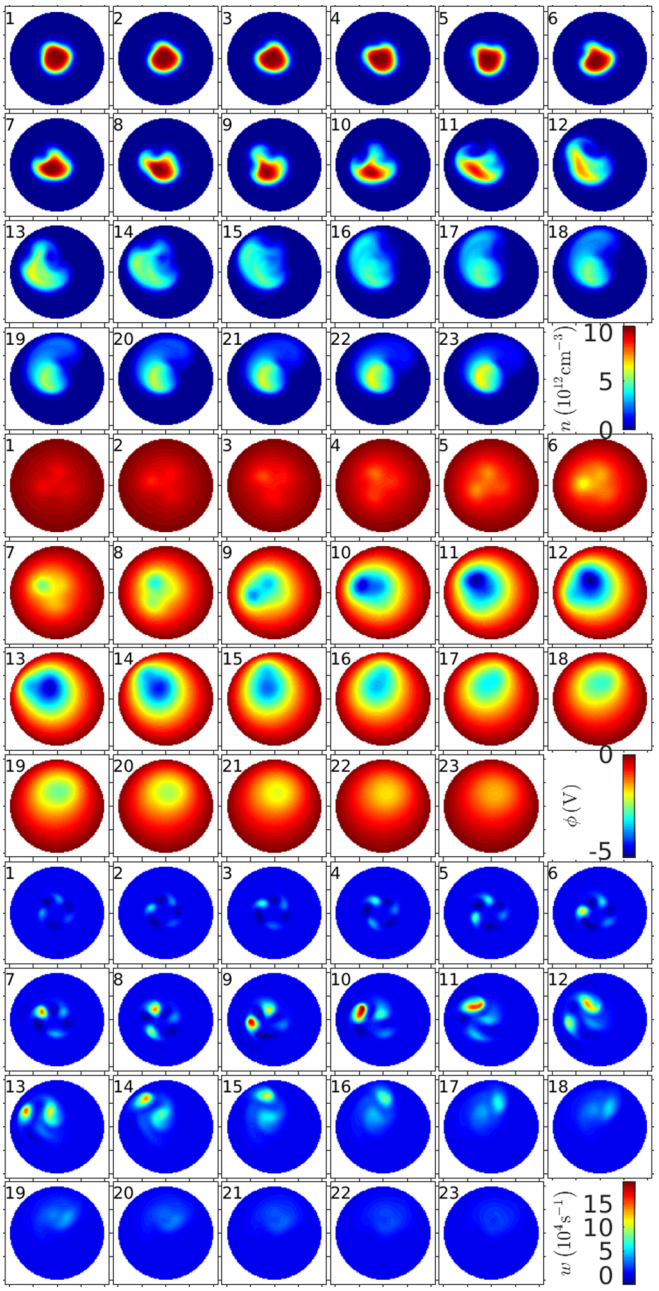

FIG. 6. Illustration of a typical avalanche with the ejection of an avaloid. With sequential numbers on the left top labeling time, the three groups of pictures show the evolution of density, electric potential, and vorticity at the entire center x-y plane of the vacuum vessel during $t = 15.6347$–16.3240 ms. The time interval between adjacent pictures is $\Delta t = 0.0313$ ms. The view angle of Fig. 1 is used.

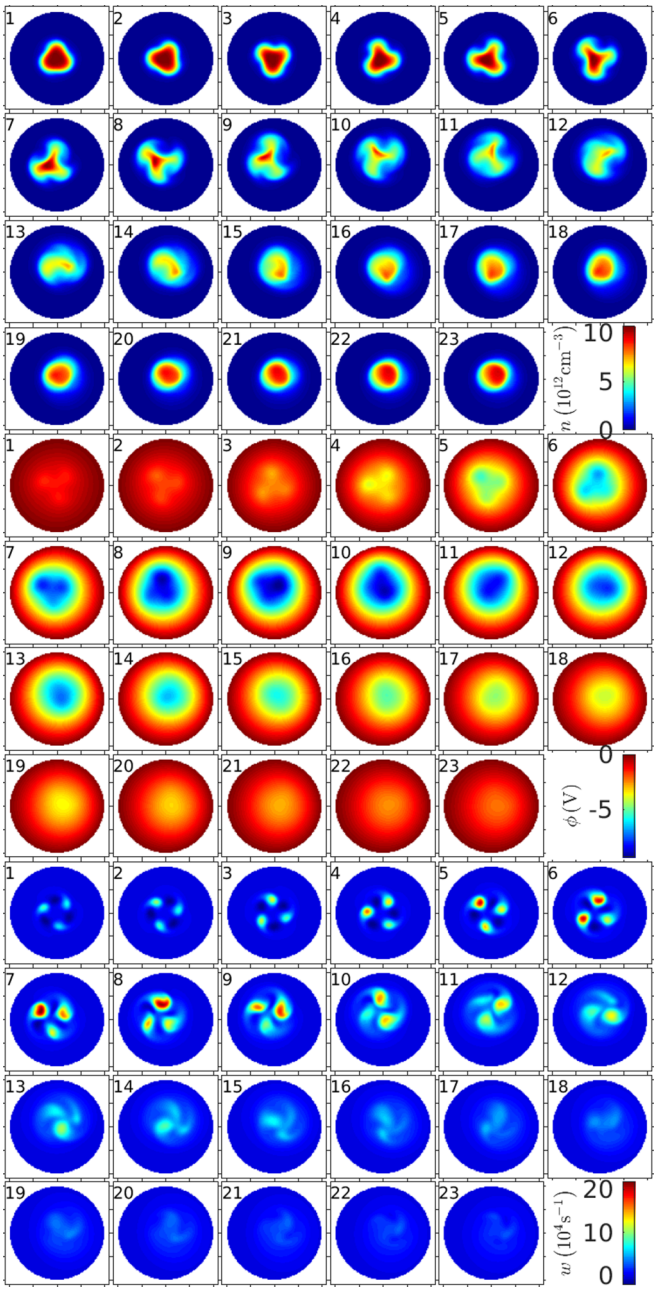

FIG. 7. Illustration of a typical avalanche without an avaloid during $t = 25.6296$–26.3189 ms.

potential transit from 3 to 1. By comparing the snapshots of density and potential, one can figure out that $0 < \xi_3\langle n, \phi\rangle < \pi/4$ and $\pi/2 < \xi_1\langle n, \phi\rangle < \pi$. This is evidence that the $m = 3$ mode is a CDW, while the $m = 1$ mode is K-H instability [16,25]. The contour lines in Figs. 6 and 7 can be regarded as the stream lines of $\boldsymbol{E} \times \boldsymbol{B}$ velocity, so that one can find how particles are convected in these snapshots.

Figure 2 can give an overview of all the transition and collapse events. When a transition happens, outward particle flux increases sharply [Fig. 2(e)], giving rise to a rapid loss of particles, which is shown in Fig. 2(d). Carrying $m = 3$ fluctuations [Fig. 2(b)], the motion of the majority of bulk plasma can be detected as a radial propagation of $m = 1$ fluctuation [Fig. 2(c)]. A collapse phase starts by the occurrence of K-H instability and ends by the exhaustion of zonal flow kinetic energy. Figures 6 and 7 also show the details of how the particle profile kept in shear flow growth phase is destructed faster and faster, and how the plasma entrained by $\boldsymbol{E} \times \boldsymbol{B}$ flow forms a structure that grows in volume, just like an avalanche. The profile is then recovered by the plasma source.

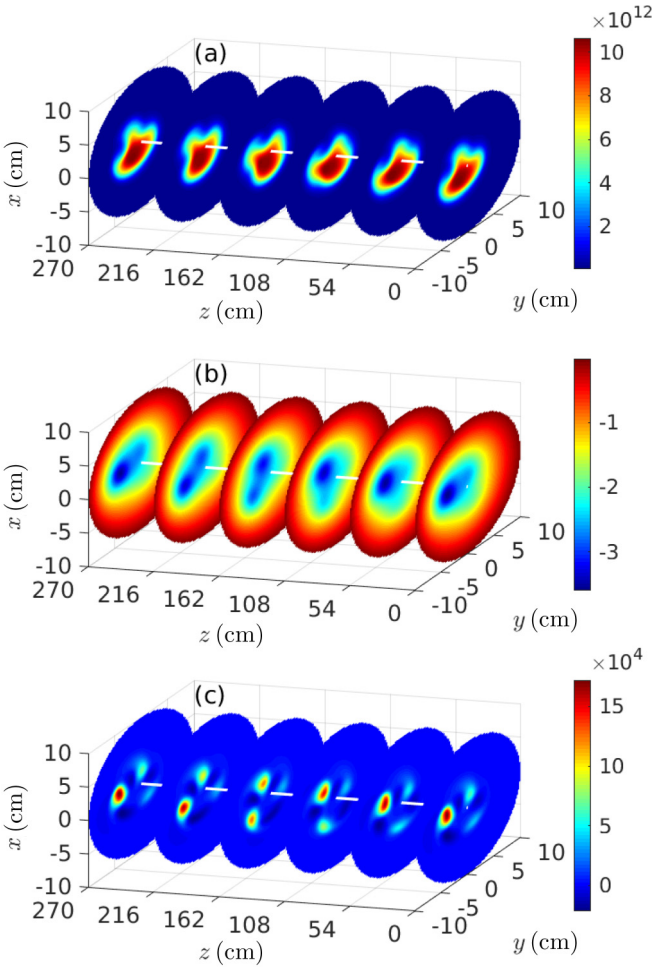

FIG. 8. 3D structures of (a) density n, (b) potential ϕ, and (c) vorticity w in the whole device when the CDW and K-H instability coexist. Contours of the fields are drawn in the x-y planes with equal intervals. The time of the snapshot is $t = 15.8540$ ms, which is the same time labeled number 8 in Fig. 6. The magnetic axis $(x, y) = (0, 0)$ is shown by the white line.

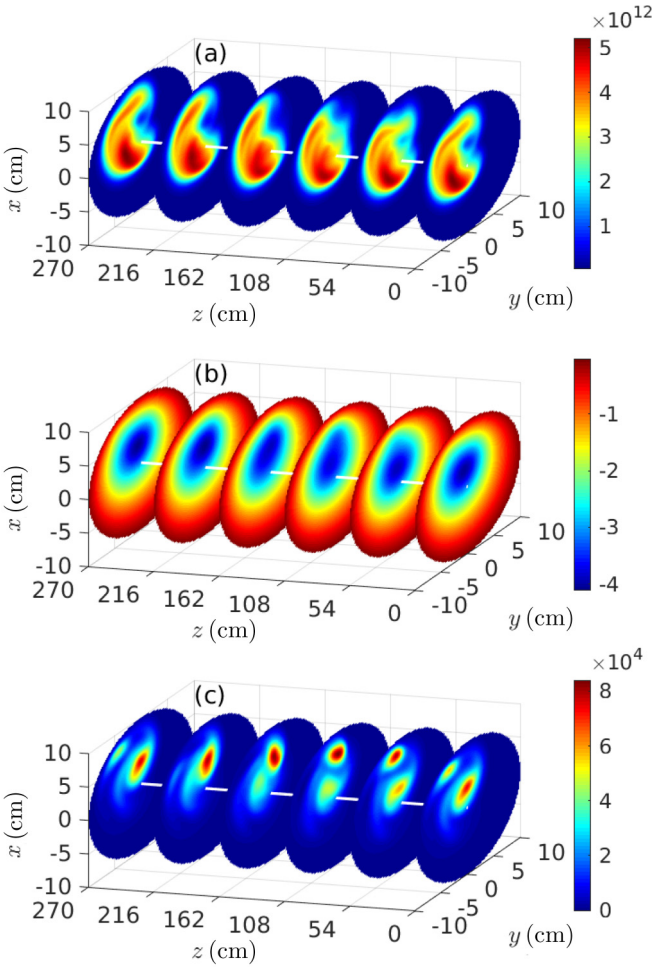

FIG. 9. 3D structure of (a) density, (b) potential, and (c) vorticity of an avaloid at $t = 16.1046$ ms, which is the same time labeled number 16 in Fig. 6. The smaller density peak in each x-y plane is the avaloid.

B. Avalanche criterion

For monotonic velocity profiles $U_x(y)$, Fjørtoft's criterion [30] shows that a necessary condition for instability is the existence of maximal vorticity $W \equiv \nabla \times \boldsymbol{U} \cdot \hat{\boldsymbol{z}} \equiv -\partial_y U_x$. To check whether some theorem like Fjørtoft's criterion also exists in our case, we check the evolution of vorticity, and two fragments of it can be found in Figs. 6 and 7. Avalanches always start at the position where local vorticity is the maximum in the whole x-y plane. To clarify that this criterion is basically z independent, we show x-y slices of the key fields at early collapse phase in Fig. 8. With the magnetic axis plotted, one can see that while the $m = 3$ CDW features $k_\parallel \sim 2\pi/L_\parallel$, the beginning of the avalanche, i.e., the $m = 1$ K-H instability, features $k_\parallel = 0$, consistent with the instability properties given in [16,25].

Realizing the vital role of maximum vorticity, we track its evolution. Every time an avalanche happens [when $\mathrm{Max}\{\langle v_{E,\theta}\rangle\}$ starts to decrease in Fig. 5(a)], the global maximum vorticity [shown by the green curves in Figs. 5(b) and 5(c)] is always in the narrow interval $1.8 \times 10^5 s^{-1} \lesssim \mathrm{Max}\{w\} \lesssim 2.2 \times 10^5 s^{-1}$, while the zonal flow contribution of vorticity [shown by the blue curves in Figs. 5(b) and 5(c)] varies a lot. Through the analysis in Sec. IV, we are convinced that this variation is proved by experiments. This means that neither zonal flow intensity nor flow shear itself can determine the onset of K-H instability. A single mode number CDW does not decide the onset of K-H instability alone too. One can realize this either by looking carefully at Fig. 2(b) or by comparing Fig. 6 with Fig. 7. We plot the global maximum vorticity contribution by local azimuthal velocity using red curves in Figs. 5(b) and 5(c) to show the importance of the radial velocity contribution. These result suggest that once the global maximum vorticity exceeds some threshold, an avalanche happens immediately. In case the criterion was affected by the avalanche itself, we filtered the $m = 1$ contribution and replotted Fig. 5. The result did not alter.

C. Relation between avalanche and avaloid

Experiments suggest that avaloids may be related to shear flow dynamics, but further study is required [7]. Here we show the relation in our simulation. We refer to the zonal flow when

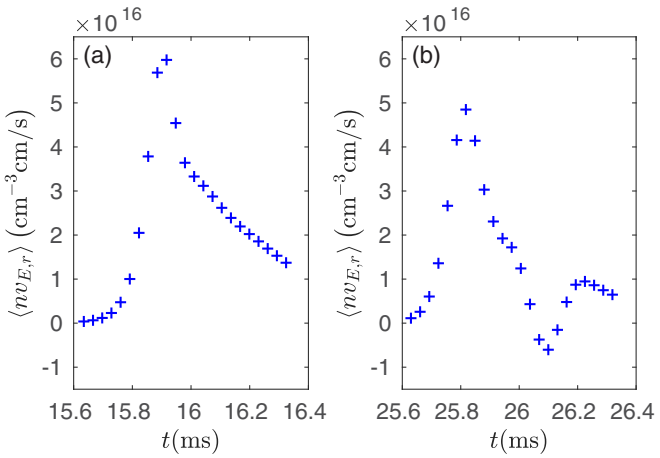

FIG. 10. Radial particle flux at $r = 1.5$ cm (a) for the snapshots in Fig. 6 (with avaloid ejection) and (b) for snapshots in Fig. 7 (without avaloid ejection).

a transition from shear flow growth phase to collapse phase happens as peak zonal flow. In Fig. 5(a) one can see that a strong peak zonal flow can be more than 100% higher than a weak one. Apart from affecting the birth time of avalanches, peak zonal flow can also determine whether the avalanche can lead to the birth of an avaloid.

Figure 6 is a typical avalanche with weak peak zonal flow. Evolutions of density and potential show how an avaloid is separated from the center dense plasma by $\boldsymbol{E} \times \boldsymbol{B}$ convection. The 3D structure of the avaloid is illustrated in Fig. 9. It distributes basically along the magnetic field line [Fig. 9(a)], but a $k_\parallel \sim 2\pi/L_\parallel$ component is still very clear, especially for the vorticity shown in Fig. 9(c). The evolution of light intensity at a fixed x-y plane in this kind of process has been observed in a previous experiment, validating our simulation in some sense [3,31].

Figure 7 is a typical avalanche with strong peak zonal flow. In this process, a large amount of ions are pulled out by $\boldsymbol{v}_E$, then rotate back in before recombination instead of being ejected out towards the chamber wall. The corresponding inward particle flux can be clearly seen in Fig. 10(b).

VI. CONCLUSION AND DISCUSSION

In conclusion, we developed an almost self-consistent code to study the global plasma evolution in CSDX $B = 1000$ G insulating endplate discharges. Analyses of CDW plasma-frame phase velocity and $\boldsymbol{E} \times \boldsymbol{B}$ velocity evolution in our simulation successfully explain the violent evolution of the azimuthal velocity of the pattern observed by a fast camera [7]. What stops zonal flow from growing and drives $m = 1$ perturbation to dominate over $m = 3$ perturbation is found to be K-H instability. The instability always happens when and where the local vorticity exceeds a fixed critical value, allowing peak shear flow to vary.

Nonlinear growth of K-H instability always leads to an avalanche, featured by the outward convection of the main plasma, explaining the experimental observation that the region outside the main plasma column ($r \lesssim 3.5$ cm) is dominated by K-H instability [16]. If zonal flow intensity just before onset of an avalanche is relatively low, an avaloid is ejected at the end of the avalanche. The avaloid distributes along a magnetic field line, but has a clear finite parallel wavelength component.

We use a code with periodic parallel boundary condition to simulate an insulating end-plate linear device. It is a compromise because a collisional sheath boundary condition is difficult to implement in the code. On the other hand, this boundary condition should make our simulation analysis for avaloids better adapted to blobs and ELM filaments in tokamaks. Although the peak vorticity for each avalanche to happen varies very slightly, they are not the same. Our preliminary analysis suggest that when the vorticity peak features a smaller perpendicular scale, peak vorticity is relatively higher. Further study is still required to find a better criterion for the birth of intermittent convective structures outside the bulk plasma.

ACKNOWLEDGMENTS

We are grateful to P. H. Diamond, G. R. Tynan, B. D. Yuan, M. Xu, Z. Yan, Z. J. Mao, C. Meng, X. Y. Wang, J. C. Li, R. J. Hong, M. Y. Wu, and Y. Zhang for useful discussions. This work was supported by the National MCF Energy R&D Program under Grant No. 2018YFE0311300.

APPENDIX A: DERIVATION OF THE MODEL EQUATIONS

We start from the equation set simplified from reduced Braginskii equations [14]:

$$\partial_t n + \nabla \cdot [n(\boldsymbol{v}_E + \boldsymbol{v}_{de} + \boldsymbol{v}_{\parallel e})] = S_n, \tag{A1}$$

$$\tfrac{3}{2} d_t p_e + \tfrac{3}{2} v_{\parallel e} \nabla_\parallel p_e + \tfrac{5}{2} p_e \nabla \cdot (\boldsymbol{v}_E + \boldsymbol{v}_{\parallel e}) = \tfrac{3}{2} S_{p_e}, \tag{A2}$$

$$\nabla \cdot \boldsymbol{j}_{\rm pol} + \nabla \cdot \boldsymbol{j}_d + \nabla_\parallel j_\parallel = 0, \tag{A3}$$

$$m_i n d_t v_{\parallel i} = -\nabla_\parallel p_e, \tag{A4}$$

$$-\nabla_\parallel p_e + en\nabla_\parallel \phi + \eta_\parallel en j_\parallel = 0, \tag{A5}$$

where

$$\boldsymbol{j}_d = -en\boldsymbol{v}_{de} = \frac{c}{B}\boldsymbol{B} \times \nabla p_e \tag{A6}$$

is the diamagnetic current,

$$\boldsymbol{j}_{\rm pol} = -\frac{enc}{B\Omega_i} d_t \nabla_\perp \phi \tag{A7}$$

is the polarization current, and

$$d_t = \partial_t + \boldsymbol{v}_E \cdot \nabla \tag{A8}$$

is the total time derivative. We have neglected $v_{\parallel i}\nabla_\parallel$ terms since they are much smaller than $\boldsymbol{v}_E \cdot \nabla$ terms.

$$\eta_\parallel = \frac{4\pi \nu_{e,i}}{\omega_{pe}^2} \tag{A9}$$

is the Spitzer resistivity. Hereafter we use the normalized symbols and omit the diffusion and damping terms. For uniform magnetic field, one can easily prove that $\nabla \cdot \boldsymbol{v}_E = \nabla \cdot (n\boldsymbol{v}_{de}) = 0$. We thus have the continuity equation

$$d_t n = -\nabla_\parallel (n v_{\parallel e}) + S_n. \tag{A10}$$

Using $p_e = nT_e$ and $n\nabla_\parallel T_e \ll T_e\nabla_\parallel n$, the electron pressure equation can be expressed as

$$\tfrac{3}{2}T_e d_t n + \tfrac{3}{2}n d_t T_e + \tfrac{3}{2}T_e\nabla_\parallel(n v_{\parallel e}) + nT_e\nabla_\parallel v_{\parallel e} = \tfrac{3}{2}S_{pe}. \tag{A11}$$

This expression can be simplified by the electron continuity equation

$$d_t T_e = -\tfrac{2}{3}T_e\nabla_\parallel v_{\parallel e} + S_{Te}. \tag{A12}$$

The ion parallel momentum equation can be simplified to

$$d_t v_{\parallel i} = -\frac{T_e}{n}\nabla_\parallel n. \tag{A13}$$

The vorticity equation is

$$\boldsymbol{\nabla}\cdot\left[n\left(\partial_t + \frac{a}{\rho_{s0}}\boldsymbol{v}_E\cdot\boldsymbol{\nabla}\right)\nabla_\perp\phi\right] = \nabla_\parallel j_\parallel. \tag{A14}$$

Define the vorticity as

$$w = \nabla_\perp^2\phi. \tag{A15}$$

Using the Boussinesq approximation [32]

$$\boldsymbol{\nabla}\cdot(n d_t\nabla_\perp\phi) = n d_t\nabla_\perp^2\phi, \tag{A16}$$

we get the vorticity equation

$$d_t w = \frac{1}{n}\nabla_\parallel j_\parallel. \tag{A17}$$

Joining Eqs. (A5) and (A9), we get the Ohm's law equation (10).

APPENDIX B: ENERGY CONSERVATION

For the verification of energy conservation of our equation set, we sum all kinds of energies and integrate over all space. Since we use periodic boundary conditions in both azimuthal and axial directions, the surface integrals only include radial contributions, and they are dropped here. In this way, all convection terms (terms in the form $\boldsymbol{v}_E\cdot\boldsymbol{\nabla}f$) vanish after volume integration since $\boldsymbol{\nabla}\cdot\boldsymbol{v}_E = 0$:

$$\int dV[\boldsymbol{v}_E\cdot\boldsymbol{\nabla}f] = \int dV[\boldsymbol{\nabla}\cdot(f\boldsymbol{v}_E)] = 0. \tag{B1}$$

Casting the temperature equation to the pressure equation and integrating by parts, we get the evolution of thermal energy

$$\partial_t\int dV\frac{3}{2}p_e = \int dV[v_{\parallel e}\nabla_\parallel p_e] + \int dV\frac{3}{2}S_{p_e}. \tag{B2}$$

Multiply the vorticity equation (A14) by ϕ yields

$$\int dV[\phi\nabla_\perp\cdot(n d_t\nabla_\perp\phi)] = \int dV[\phi\nabla_\parallel j_\parallel]. \tag{B3}$$

Integrating by parts, we get

$$\int dV\left[\frac{n}{2}d_t(\nabla_\perp\phi)^2\right] = \int dV[j_\parallel\nabla_\parallel\phi]. \tag{B4}$$

Using the continuity equation (A1), one can easily prove that

$$\begin{aligned}\int dV\left[n d_t f\right] &= \int dV[n\partial_t f + n\boldsymbol{v}_E\cdot\boldsymbol{\nabla}f]\\ &= \int dV[n\partial_t f - f\boldsymbol{\nabla}\cdot(n\boldsymbol{v}_E)]\\ &= \int dV[n\partial_t f + f\partial_t n]\\ &= \int dV[\partial_t(nf)].\end{aligned} \tag{B5}$$

Furthermore, the local ion kinetic energy is

$$\frac{n}{2}\boldsymbol{v}_E^2 = \frac{n}{2}(\boldsymbol{b}\times\boldsymbol{\nabla}\phi)^2 = \frac{n}{2}(\boldsymbol{\nabla}_\perp\phi)^2. \tag{B6}$$

We thus get the evolution of perpendicular kinetic energy,

$$\partial_t\int dV\left[\frac{n}{2}\boldsymbol{v}_E^2\right] = \int dV[j_\parallel\nabla_\parallel\phi]. \tag{B7}$$

Multiplying the ion momentum equation Eq. (A13) by $v_{\parallel i}$, we get the evolution of parallel kinetic energy,

$$\partial_t\int dV\left[\frac{n}{2}v_{\parallel i}^2\right] = \int dV[-v_{\parallel i}\nabla_\parallel p_e]. \tag{B8}$$

Adding Eqs. (B2), (B7), and (B8), we can get the total energy evolution using Eqs. (A5) and (12):

$$\partial_t\int dV\left[\frac{3}{2}p_e + \frac{n}{2}\left(\boldsymbol{v}_E^2 + v_{\parallel i}^2\right)\right] = \int dV\left[\frac{3}{2}S_{p_e} - \eta_\parallel j_\parallel^2\right]. \tag{B9}$$

So the system energy is controlled by an external energy source and a resistive dissipation, since we did not include Ohmic heating in the electron pressure equation.

APPENDIX C: ESTIMATION OF PERPENDICULAR MAGNETIC PERTURBATIONS

We write the total magnetic field in the form $\boldsymbol{B} = B\hat{\boldsymbol{z}} + \boldsymbol{B}_\perp$, where $B\hat{\boldsymbol{z}}$ is the dominant uniform magnetic field and $\boldsymbol{B}_\perp = B_r\hat{\boldsymbol{r}} + B_\theta\hat{\boldsymbol{\theta}}$ represents the magnetic perturbations perpendicular to it in the cylindrical device. These perturbations are estimated to be much lower than B by solving $\boldsymbol{\nabla}\times\boldsymbol{B}_\perp = j_\parallel\hat{\boldsymbol{z}}$ in the code (Fig. 11). Consequently, $\boldsymbol{B} = B\hat{\boldsymbol{z}}$ is a good approximation and $\boldsymbol{B}_\perp$ never enters Eqs. (1) to (4).

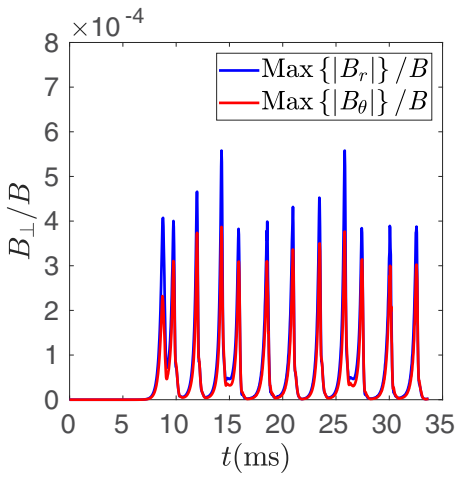

FIG. 11. Global maximum amplitude of magnetic perturbations perpendicular to the dominant magnetic field direction.

[1] M. Endler, J. Nucl. Mater. **266-269**, 84 (1999).

[2] K. Kamiya, N. Asakura, J. Boedo, T. Eich, G. Federici, M. Fenstermacher, K. Finken, A. Herrmann, J. Terry, A. kirk, B. Koch, A. Loarte, R. Maingi, R. Maqueda, E. Nardon, N. Oyama, and R. Sartori, Plasma Phys. Controlled Fusion **49**, S43 (2007).

[3] G. Y. Antar, J. H. Yu, and G. Tynan, Phys. Plasmas **14**, 022301 (2007).

[4] L. Cui, A. Ashourvan, S. C. Thakur, R. Hong, P. H. Diamond, and G. R. Tynan, Phys. Plasmas **23**, 055704 (2016).

[5] A. Kirk, N. Asakura, J. A. Boedo, M. Beurskens, G. F. Counsell, T. Eich, W. Fundamenski, A. Herrmann, Y. Kamada, A. W. Leonard, S. Lisgo, A. Loarte, N. Oyama, R. A. Pitts, A. Schmid, and H. R. Wilson, J. Phys. Conf. Ser. **123**, 012011 (2008).

[6] M. Xu, G. R. Tynan, P. H. Diamond, C. Holland, J. H. Yu, and Z. Yan, Phys. Rev. Lett. **107**, 055003 (2011).

[7] Z. Yan, G. R. Tynan, C. Holland, M. Xu, S. H. Müller, and J. H. Yu, Phys. Plasmas **17**, 032302 (2010).

[8] C. Holland, G. R. Tynan, J. H. Y. A. James, D. Nishijima, M. Shimada, and N. Taheri, Plasma Phys. Controlled Fusion **49**, A109 (2007).

[9] D. A. D'Ippolito, D. A. Russell, J. R. Myra, S. C. Thakur, G. R. Tynan, and C. Holland, Phys. Plasmas **19**, 102301 (2012).

[10] P. Vaezi, C. Holland, S. C. Thakur, and G. R. Tynan, Phys. Plasmas **24**, 042306 (2017).

[11] P. Vaezi, C. Holland, S. C. Thakur, and G. R. Tynan, Phys. Plasmas **24**, 092310 (2017).

[12] P. W. Xi, X. Q. Xu, X. G. Wang, and T. Y. Xia, Phys. Plasmas **19**, 092503 (2012).

[13] P. W. Xi, X. Q. Xu, and P. H. Diamond, Phys. Rev. Lett. **112**, 085001 (2014).

[14] A. Zeiler, J. F. Drake, and B. Rogers, Phys. Plasmas **4**, 2134 (1997).

[15] Z. Yan, J. H. Yu, C. Holland, M. Xu, S. H. Müller, and G. R. Tynan, Phys. Plasmas **15**, 092309 (2008).

[16] S. C. Thakur, C. Brandt, L. Cui, J. J. Gosselin, A. D. Light, and G. R. Tynan, Plasma Sources Sci. Technol. **23**, 044006 (2014).

[17] R. Hong, J. C. Li, S. Chakraborty Thakur, R. Hajjar, P. H. Diamond, and G. R. Tynan, Phys. Rev. Lett. **120**, 205001 (2018).

[18] J. C. Li, P. H. Diamond, X. Q. Xu, and G. R. Tynan, Phys. Plasmas **23**, 052311 (2016).

[19] P. C. Stangeby, *The Plasma Boundary of Magnetic Fusion Devices* (CRC, Boca Raton, FL, 2000).

[20] B. N. Rogers and P. Ricci, Phys. Rev. Lett. **104**, 225002 (2010).

[21] D. M. Fisher, B. N. Rogers, G. D. Rossi, D. S. Guice, and T. A. Carter, Phys. Plasmas **22**, 092121 (2015).

[22] Z. Yan, M. Xu, P. H. Diamond, C. Holland, S. H. Müller, G. R. Tynan, and J. H. Yu, Phys. Rev. Lett. **104**, 065002 (2010).

[23] B. Li, X. Y. Wang, C. K. Sun, C. Meng, A. Zhou, and D. Liu, Phys. Plasmas **24**, 055905 (2017).

[24] R. F. Ellis, E. Marden-Marshall, and R. Majeski, Plasma Phys. **22**, 113 (1980).

[25] D. L. Jassby, Phys. Fluids **15**, 1590 (1972).

[26] S. C. Thakur, J. J. Gosselin, J. McKee, E. E. Scime, S. H. Sears, and G. R. Tynan, Phys. Plasmas **23**, 082112 (2016).

[27] S. Chakraborty Thakur, M. Xu, P. Manz, N. Fedorczak, C. Holland, and G. R. Tynan, Phys. Plasmas **20**, 012304 (2013).

[28] M. Xu, G. R. Tynan, C. Holland, Z. Yan, S. H. Muller, and J. H. Yu, Phys. Plasmas **17**, 032311 (2010).

[29] Ö. D. Gürcan and P. H. Diamond, J. Phys. A: Math. Theor. **48**, 293001 (2015).

[30] P. J. Schmid and D. S. Henningson, *Stability and Transition in Shear Flows*, Applied Mathematical Sciences Vol. 142 (Springer, New York, 2001).

[31] S. H. Müller, C. Theiler, A. Fasoli, I. Furno, B. Labit, G. R. Tynan, M. Xu, Z. Yan, and J. H. Yu, Plasma Phys. Controlled Fusion **51**, 055020 (2009).

[32] P. Ricci, F. D. Halpern, S. Jolliet, J. Loizu, A. Mosetto, A. Fasoli, I. Furno, and C. Theiler, Plasma Phys. Controlled Fusion **54**, 124047 (2012).